THE JOURNAL OF BIOLOGICAL CHEMISTRY VOL. 289, NO. 52, pp. 35907–35917, December 26, 2014
Published in the U.S.A.

Structural Basis for the De-*N*-acetylation of Poly-β-1,6-*N*-acetyl-D-glucosamine in Gram-positive Bacteria*

Received for publication, September 11, 2014, and in revised form, October 29, 2014 Published, JBC Papers in Press, October 30, 2014, DOI 10.1074/jbc.M114.611400

Dustin J. Little[‡§1], Natalie C. Bamford[‡§2], Varvara Pokrovskaya[¶], Howard Robinson[‖], Mark Nitz[¶3], and P. Lynne Howell[‡§4]

From the [‡]Program in Molecular Structure and Function, Research Institute, The Hospital for Sick Children, Toronto, Ontario M5G 1X8, Canada, [§]Department of Biochemistry, University of Toronto, Toronto, Ontario M5S 1A8, Canada, [¶]Department of Chemistry, University of Toronto, Toronto, Ontario M5S 3H6, Canada, and [‖]Photon Sciences Division, Brookhaven National Laboratory, Upton, New York 11973-5000

Background: IcaB is a poly-β-1,6-*N*-acetyl-D-glucosamine (PNAG) deacetylase required for polysaccharide intercellular adhesion-dependent biofilm formation by staphylococci.
Results: The structure of *Ammonifex degensii* IcaB has been determined and its catalytic mechanism and localization characterized.
Conclusion: IcaB is a membrane-associated PNAG deacetylase that uses an altered catalytic mechanism relative to other family 4 carbohydrate esterases.
Significance: First structural characterization of a Gram-positive PNAG deacetylase.

Exopolysaccharides are required for the development and integrity of biofilms produced by a wide variety of bacteria. In staphylococci, partial de-*N*-acetylation of the exopolysaccharide poly-β-1,6-*N*-acetyl-D-glucosamine (PNAG) by the extracellular protein IcaB is required for biofilm formation. To understand the molecular basis for PNAG de-*N*-acetylation, the structure of IcaB from *Ammonifex degensii* ($IcaB_{Ad}$) has been determined to 1.7 Å resolution. The structure of $IcaB_{Ad}$ reveals a $(\beta/\alpha)_7$ barrel common to the family four carbohydrate esterases (CE4s) with the canonical motifs circularly permuted. The metal dependence of $IcaB_{Ad}$ is similar to most CE4s showing the maximum rates of de-*N*-acetylation with Ni^{2+}, Co^{2+}, and Zn^{2+}. From docking studies with β-1,6-GlcNAc oligomers and structural comparison to PgaB from *Escherichia coli*, the Gram-negative homologue of IcaB, we identify Arg-45, Tyr-67, and Trp-180 as key residues for PNAG binding during catalysis. The absence of these residues in PgaB provides a rationale for the requirement of a C-terminal domain for efficient deacetylation of PNAG in Gram-negative species. Mutational analysis of conserved active site residues suggests that IcaB uses an altered catalytic mechanism in comparison to other characterized CE4 members. Furthermore, we identified a conserved surface-exposed hydrophobic loop found only in Gram-positive homologues of IcaB. Our data suggest that this loop is required for membrane association and likely anchors IcaB to the membrane during polysaccharide biosynthesis. The work presented herein will help guide the design of IcaB inhibitors to combat biofilm formation by staphylococci.

Staphylococcus epidermidis is a Gram-positive commensal bacteria that is the most prevalent organism found in indwelling medical-device-related bacterial infections (1). Nosocomial *S. epidermidis* infections are often caused by the bacteria forming a biofilm on biomaterials (2, 3). A biofilm is a cluster of microcolonies encapsulated within self-produced extracellular polymeric substances (4, 5). The components of the biofilms can be quite diverse but are generally composed of proteinaceous adhesins, nucleic acids, and exopolysaccharides (6–8). Exopolysaccharides are important for biofilm structure and architecture by allowing the diffusion of nutrients in and waste products out (4, 9). Exopolysaccharides have also been shown to function as adhesins, reduce the diffusion of antibiotics into the biofilm, and provide a barrier against phagocytosis (7, 10).

The conserved exopolysaccharide known as polysaccharide intercellular adhesin was originally identified in the biofilms of *S. epidermidis* (11) and *Staphylococcus aureus* (12) and has now been shown to be produced by various Gram-negative bacteria (13–19) and higher eukaryotes (20). Polysaccharide intercellular adhesin is synthesized as a β-1,6-linked poly-*N*-acetyl-D-glucosamine (PNAG)[5] polymer and subsequently modified by partially de-*N*-acetylation and/or *O*-succinylation. In *S. epidermidis,* de-*N*-acetylated PNAG (dPNAG) production is dependent on the four-gene operon, *icaADBC* (21). IcaA, which is predicted to contain multiple transmembrane domains and a large cytosolic family 2 glycosyltransferase domain, is thought to be responsible for the production of PNAG and its translo-

* This work was supported by Canadian Institutes of Health Research Grants 43998 (to P. L. H.) and 89708 (to M. N.).
The atomic coordinates and structure factors (code 4WCJ) have been deposited in the Protein Data Bank (http://wwpdb.org/).
[1] Supported in part by graduate scholarships from the University of Toronto, the Ontario Graduate Scholarship Program, and Canadian Institutes of Health Research.
[2] Supported in part by graduate scholarships from the Natural Sciences and Engineering Research Council of Canada and Mary H. Beatty and Dr. James A. and Connie P. Dickson Scholarships from the University of Toronto.
[3] To whom correspondence may be addressed. Tel.: 416-946-0640; E-mail: mnitz@chem.utoronto.ca.
[4] Recipient of a Canada Research Chair. To whom correspondence may be addressed. Tel.: 416-813-5378; E-mail: howell@sickkids.ca.

[5] The abbreviations used are: PNAG, poly-β-1,6-*N*-acetyl-D-glucosamine; dPNAG, de-*N*-acetylated PNAG; CE4, family 4 carbohydrate esterase; Bis-Tris, 2-[bis(2-hydroxyethyl)amino]-2-(hydroxymethyl)propane-1,3-diol.

cation across the membrane (21, 22). IcaD is a small integral membrane protein that significantly increases PNAG biosynthesis when co-expressed with IcaA and potentially aids in PNAG translocation across the membrane (22). IcaC is an integral membrane protein that was originally predicted to be responsible for exporting mature long-chain PNAG (21). However, the proposed function of IcaC has recently been revisited (23). Bioinformatics analysis predicts that IcaC contains 10 transmembrane helices and is a member of a large acetyltransferase family, suggesting it plays a role in the *O*-modification of PNAG during biosynthesis (23). The presence of succinate groups on PNAG isolated from *S. epidermidis* (24) and *S. aureus* (25) supports the role of IcaC as an *O*-succinyltransferase. IcaB is an extracellular protein that is responsible for the partial de-*N*-acetylation of PNAG (26), a requirement for surface retention of the polymer. Furthermore, Δ*icaB* strains of *S. epidermidis* and *S. aureus* are unable to de-*N*-acetylate PNAG, do not form biofilms *in vitro*, and have highly attenuated virulence in a murine model for an indwelling medical device-related infection and bacteremia, respectively (26, 27). IcaB is a member of the family 4 carbohydrate esterases (CE4s) and has sequence homology (22% identity) to the N-terminal de-*N*-acetylase domain of *Escherichia coli* PgaB ($PgaB^{22-309}$) (28). Recent characterization of PgaB has shown that its C-terminal domain ($PgaB^{310-672}$) is required for binding and de-*N*-acetylation of PNAG, as the isolated $PgaB^{22-309}$ de-*N*-acetylase domain is inactive (29).

Herein we present the first structure of IcaB from *Ammonifex degensii* ($IcaB_{Ad}$). The identification of key active site residues that are conserved within Gram-positive homologues provides a structural rationale for why IcaB, unlike its Gram-negative counterpart PgaB, does not require a C-terminal domain for enzymatic activity (29). Biochemical characterization of $IcaB_{Ad}$ and *S. epidermidis* IcaB ($IcaB_{Se}$) suggests the extracellular enzymes are membrane-associated and are anchored by a conserved hydrophobic loop. Furthermore, we provide the first mutational analysis of a PNAG deacetylase. The mutagenesis data suggests that the circular permutation of the CE4 motifs alters the enzymatic mechanism relative to other CE4s members (30, 31).

EXPERIMENTAL PROCEDURES

Cloning, Expression, and Purification of $IcaB_{Se}$ Constructs—The plasmid UT032 (32), which contains a codon-optimized version of the *icaB* gene from *S. epidermidis* (encoding residues 30–289) in pET16b, was used as a template to subclone *icaB* into the pET28a expression vector (Novagen). Inverse PCR was used with the forward and reverse primers GGGCATATGGCGAACGAAGAAAACAAAAAACTG and GGCTCGAGTCATTTTTCTTCGTCGAAACCGTCCC, which contain an NdeI and XhoI site, respectively, to yield plasmid pET28-$IcaB_{Se}^{30-289}$. The resulting plasmid encodes a thrombin-cleavable N-terminal hexahistidine tag fused to $IcaB_{Se}^{30-289}$. The D120N and H50A mutants of $IcaB_{Se}^{30-289}$ were generated using the QuikChange lightning site-directed mutagenesis kit (Agilent Technologies) as per the manufacturer's instructions with the forward and reverse primers GGATCAACTTCAACGACATGGACCAGACCATCTAC and GTAGATGGTCTGGTCCATGTCGTTGAAGTTGATCC and CTGGCGCTGAACTACGCCCGTGTTCG and CGAACACGGGCGTAGTTCAGCGCCAG, respectively. The hydrophobic loop deletion mutant of $IcaB_{Se}^{30-289}$ ($IcaB_{Se}^{30-289\Delta loop}$) was generated in three successive steps using the QuikChange lightening site-directed mutagenesis kit with the following modifications; (i) the denaturing and annealing duration steps were 30 s; (ii) the annealing temperature was 55 °C; (iii) the protocol was completed with 25 cycles. The first step deleted residues 54–72 using the forward and reverse primers CTACCACCGTGTTCGTAACTACTCTGTTACCG and CGGTAACAGAGTAGTTACGAACACGGTGGTAG. The second step inserted residues AAG after Arg-53 using the forward and reverse primers GAACTACCACCGTGTTCGTGCGGCGGGTGAAATCAAAAACTACTCTG and CAGAGTAGTTTTTGATTTCACCCGCCGCACGAACACGGTGGTAGTTC. The third step inserted residues EI to yield AAEIG after Arg-53 using the forward and reverse primers CCACCGTGTTCGTGCGGCGGAAATTGGTGAAATCAAAAAC and GTTTTTGATTTCACCAATTTCCGCCGCACGAACACGGTGG. The resulting construct $IcaB_{Se}^{30-289\Delta loop}$ contains the mutations K54A, K55A, and K72G with residues 56–69 deleted.

The following protocol was used to express and purify all the $IcaB_{Se}$ constructs. *E. coli* BL21-CodonPlus cells transformed with the appropriate plasmid were grown in 1 liter of Luria-Bertani (LB) medium with 50 μg/ml kanamycin at 37 °C to an absorbance at 600 nm (A_{600}) of ~0.4–0.5 and moved to 25 °C. When the cultures reached an A_{600} of ~0.6–0.7, protein expression was induced by the addition of isopropyl-D-1-thio-galactopyranoside to a final concentration of 1 mM. The cells were incubated for 3 h at 25 °C, harvested by centrifugation at 5000 × *g* for 20 min, and frozen on dry ice. Cell pellets were thawed and resuspended in 40 ml of lysis buffer (50 mM HEPES, pH 7.0, 1 M NaCl, 10 mM imidazole, 5% (v/v) glycerol, and one complete mini protease inhibitor mixture tablet (Roche Applied Science)). Resuspended cells were disrupted with three passes through an Emulsiflex-c3 (Avestin) at 15,000 p.s.i., and cell debris was removed by centrifugation at 31,000 × *g* for 30 min. The resulting supernatant was passed over a gravity column containing 3 ml of nickel-nitrilotriacetic acid resin (Qiagen) that was pre-equilibrated with buffer A (20 mM HEPES, pH 7.0, 1 M NaCl, 10 mM imidazole). Bound protein was washed with 10 column volumes of buffer A, 3 column volumes of buffer A with 20 mM imidazole, and eluted with 5 column volumes of buffer A with 250 mM imidazole. The eluted fraction was concentrated using a 10-kDa cut-off Amicon ultrafiltration device (EMD Millipore) and further purified and buffer-exchanged into buffer B (20 mM HEPES, pH 7.0, and 1 M NaCl) by gel filtration chromatography using a HiLoad 16/60 Superdex 200 prep-grade column (GE Healthcare). The purified $IcaB_{Se}$ constructs were >95% pure as judged by SDS-PAGE and stable for ~1 week at 4 °C.

Cloning, Expression, and Purification of $IcaB_{Ad}$ Constructs—A codon-optimized version of *A. degensii icaB* (GeneArt Invitrogen) was used as the template to subclone mature *icaB* into the pET28a expression vector (Novagen). Inverse PCR was used with the forward and reverse primers GGGCATATGGAAAGTCCGCGTACACCGGCAGGC and GGCTCGAGTTACGG-

GCTTGCCTGTGCCCATGCT, which contain an NdeI and XhoI site, respectively, to yield plasmid pET28-IcaB$_{Ad}^{23-280}$. The resulting plasmid encodes a thrombin-cleavable N-terminal hexahistidine tag fused to IcaB$_{Ad}$ residues 23–280. The hydrophobic loop deletion mutant of IcaB$_{Ad}^{23-280}$ (IcaB$_{Ad}^{23-280\Delta loop}$) was generated in one step using the same protocol as described above for IcaB$_{Se}^{30-289\Delta loop}$ using the forward and reverse primers CATCGTGTTCTGCCGAGCAGCCGTTATGCAATTAGC and GCTAATTGCATAACGGCTGCTCGGCAGAACAC-GATG. The D114N and H44A mutants of IcaB$_{Ad}^{23-280\Delta loop}$ were generated in the same manner as described above for IcaB$_{Se}^{30-289}$ using the forward and reverse primers GCTT-GTACTGGTTACCTTTAATGATGGTGATCTGAGCG and CGCTCAGATCACCATCATTAAAGGTAACCAGT-ACAAGC and GTTCTGTGTTATGCTCGTGTTCTGC-CGAG and CTCGGCAGAACACGAGCATAACACAG-AAC, respectively.

All the IcaB$_{Ad}$ constructs were expressed and purified as described for IcaB$_{Se}$ with the following modifications; (i) cultures were moved prior to and induced at 18 °C for 16 h before being harvested; (ii) for the purification of IcaB$_{Ad}^{23-280}$ the lysis buffer, buffer A, and buffer B contained 8, 4, and 1 mM CHAPS detergent, respectively; (iii) tris(2-carboxyethyl) phosphine was included in the lysis buffer and buffer A; (iv) 2 mM 2-mercaptoethanol was included in buffer B for fluorescamine assays; (v) buffer C (Tris, pH 7.0, 0.6 M NaCl, and 5 mM DTT) was used during gel-filtration chromatography purification of IcaB$_{Ad}^{23-280\Delta loop}$ for crystallization trials. The purified IcaB$_{Ad}$ constructs were >95% pure as judged by SDS-PAGE and stable for ~2 weeks at 4 °C.

Crystallization, Data Collection, and Structure Solution—Purified IcaB$_{Ad}^{23-280\Delta loop}$ was concentrated to ~9–10 mg/ml and screened for crystallization conditions at 20 °C using hanging-drop vapor diffusion in 48-well VDX plates (Hampton Research) and the MCSG 1–4 sparse matrix suites (Microlytic). An initial crystallization hit was obtained in condition #72 from the MCSG-1 suite (30% (w/v) PEG 2000 monomethyl ether and 0.1 M potassium thiocyanate). Homemade grid-optimized screens failed to reproduce crystals, so a stock solution of MCSG-1 #72 was purchased from Microlytic. The entire 48-well plates were setup using the stock solution, and on average 3–5 drops per plate produced crystals in 1 month. One irregular shaped crystal (crystal 1) with dimensions of 50 × 50 × 20 μM was suitable for diffraction studies. After four months of incubation of the initial crystallization trials, bipyramidal-shaped crystals with dimensions of 60 × 30 × 30 μM also formed in condition #24 from the MCSG-1 suite (28% (w/v) PEG 2000 monomethyl ether, 0.1 M bis(2-hydroxyethyl)aminotris(hydroxymethyl) methane (Bis-Tris), pH 6.5) and were suitable for diffraction studies (crystal 2). The crystals were cryoprotected for 5 s in reservoir solution supplemented with 20% (v/v) ethylene glycol before vitrification in liquid nitrogen. All data were collected on beam line X29 at the National Synchrotron Light Source (Table 1). A total of 360 images of 1° oscillation were collected for crystal 1 and crystal 2 on an ADSC Quantum-315r detector with a 300- or 260-mm crystal-to-detector distance, respectively, and an exposure time of 0.4 s per image. The data were indexed, integrated, and scaled using HKL2000 (33). The structure was determined for crystal 1 by molecular replacement with PHENIX AutoMR (34) using a truncated version of the N-terminal domain of PgaB$^{42-655}$ (PDB ID 4F9D) as a search model with residues 43–48, 56–70, 146–160, 191–222, 276–288, and 310–646 removed from the model. The resulting electron density map enabled PHENIX AutoBuild (34) to build ~40% of the protein. The remaining residues were built manually in COOT (35) and alternated with refinement using PHENIX.REFINE (34). The model from crystal 1 was then used to solve the structure of crystal 2 using molecular replacement, with manual model building and refinement as describe previously. Translation/Libration/Screw (TLS) groups were used during refinement and determined automatically using the TLSMD web server (36, 37). Structure figures were generated using the PyMOL Molecular Graphics System (DeLano Scientific), and quantitative electrostatics were calculated using PDB2PQR (38, 39) and APBS (40). Programs used for crystallographic data processing and analysis were accessed through SBGrid (41).

X-ray Absorption Spectroscopy Metal Analysis—X-ray absorption spectroscopy (XAS) was carried out on IcaB$_{Ad}^{23-280\Delta loop}$ crystal 1 on beam line X29, National Synchrotron Light Source. Two datasets were collected, at wavelengths of 1.2698 and 1.2964 Å, above and below the Zn^{2+} absorption edge, respectively. The data were collected, indexed, integrated, and scaled as described above. Anomalous electron density maps were generated for both datasets using sfall in the CCP4 suite (42).

Docking Studies—The binding of β-1,6-(GlcNAc)$_3$ and β-1,6-(GlcNAc)$_5$ were investigated using AutoDock Vina 1.1.2 (43). The structure files for β-1,6-(GlcNAc)$_3$ and β-1,6-(GlcNAc)$_5$ were constructed using the web-based Glycam Biomolecule Builder (44). Receptor and ligand Protein Data Bank files were prepared for docking using scripts provided from MGLTools 1.5.6 (45). Docking was conducted with a grid spacing of 0.37 and xyz of 23 × 19 × 18 using a rigid receptor with 10 poses computed. The top productive pose (*N*-Ac group bound to the zinc ion) for β-1,6-(GlcNAc)$_3$ and β-1,6-(GlcNAc)$_5$ had scores of −7.2 kcal/mol and −6.0 kcal/mol, respectively.

Preparation of PNAG Oligomers—β-1,6-GlcNAc oligomers were synthesized and purified, and their identities were confirmed as outlined previously (46). The β-1,6-GlcNAc oligomers were stored as lyophilized powders at room temperature and dissolved with deionized water for use in assays. Accurate oligomer concentrations were determined by ^{1}H NMR using dimethylformamide as an internal standard.

Fluorescamine Enzyme Activity Assays—The de-*N*-acetylation activity of various IcaB constructs and mutants on PNAG oligomers was determined by labeling the free amine groups produced during catalysis using a fluorescamine-based assay (47). The assay was performed as described previously (32) with the following modification; BRAND black 96-well plates were used for fluorescence measurements using a SpectraMax M2 plate reader from Molecular Devices (Sunnyvale, CA). For the metal-preference assay, IcaB$_{Ad}^{23-280\Delta loop}$ (30 μM) in buffer B was preincubated in the presence of various divalent metals as chloride salt solutions (30 μM) or metal chelators (1 mM) at room temperature for 30 min. The mixture was then incubated

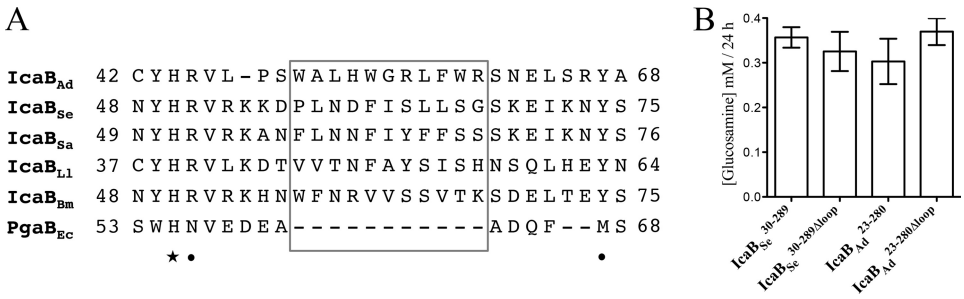

FIGURE 1. **A hydrophobic loop in IcaB is not required for PNAG de-*N*-acetylation.** *A*, sequence alignment of IcaB from *A. degensii* KC4 (*IcaB$_{Ad}$*), *S. epidermidis* RP62A (*IcaB$_{Se}$*), *S. aureus* MRSA252 (*IcaB$_{Sa}$*), *Lactococcus lactis* Il1403 (*IcaB$_{Ll}$*), *Bacillus megaterium* WSH-002 (*IcaB$_{Bm}$*), and *E. coli* K-12 PgaB (*PgaB$_{Ec}$*) reveals the presence of a conserved hydrophobic loop in Gram-positive homologues (*gray box*). Residue numbers are listed before and after the respective sequence. The ⋆ and ● represent the catalytic histidine and active site pocket residues conserved only within Gram-positive homologues, respectively. *B*, fluorescamine assays comparing the de-*N*-acetylation activity of IcaB$_{Se}^{30-289}$, IcaB$_{Se}^{30-289\Delta loop}$, IcaB$_{Ad}^{23-280}$, and IcaB$_{Ad}^{23-280\Delta loop}$ suggest that the hydrophobic loop is not required for PNAG de-*N*-acetylation. *Bars* represent triplicate experiments with S.D.

at 37 °C for 24 h with 50 mM PNAG tetramer and pentamer oligomer mixture, and the amount of de-*N*-acetylation was quantified using the fluorescamine assay. For the pH dependence of the enzymes, reactions were measured between pH 5.0 and 9.0 using a three-component MES-HEPES-borate buffer system (100 mM) and NaCl (500 mM). Reactions were conducted at 37 °C using 30 μM enzyme, 30 μM $CoCl_2$ or $NiCl_2$, and 50 mM PNAG tetramer and pentamer oligomer mixture. A glucosamine standard curve was used to quantify the observed de-*N*-acetylation activity.

Membrane Binding Assays—Staphylococcus carnosus was grown in 1 liter of LB media at 37 °C for 16 h, and cells were harvested at 5000 × *g* for 20 min. The cell pellet was resuspended and digested with 20 mg/ml lysozyme in 25 ml of buffer D (50 mM HEPES, pH 8.0, 300 mM NaCl, and 2 mM tris(2-carboxyethyl) phosphine) for 90 min at 25 °C. Digested cells were then further disrupted with five passes through an Emulsiflex-c3 at 25,000 p.s.i., and cell debris was removed by centrifugation at 31,000 × *g* for 30 min. Membranes were then isolated by centrifugation at 200,000 × *g* for 1 h. Total membranes were weighed and resuspended using a hand press in buffer D with the addition of a protease tablet to a concentration of 75–80 mg/ml. For each reaction a 500 μl volume was used with 10 μM concentrations of protein incubated with ~35 mg of membranes in buffer D. The reactions were incubated for 2 h at 4 °C, and membrane fractions were isolated by centrifugation at 100,000 × *g* for 45 min. Supernatants were removed, and the pellets were washed 3 times and then resuspended with 500 μl buffer D. The supernatant and resuspended pellet fractions were analyzed by Western blot using α-His_6 conjugated to alkaline phosphatase (Sigma) and developed with nitro blue tetrazolium chloride/5-bromo-4-chloro-3′-indolyphosphate *p*-toluidine salt reagent (Thermo Scientific Pierce).

RESULTS

Generation of Stable IcaB Constructs—The production and purification of IcaB from Gram-positive bacteria for functional characterization purposes has proven to be challenging. Our group recently reported the generation of the first stable soluble IcaB construct from *S. epidermidis* (32) using a codon-optimized gene, induction and expression at 10 °C, and with high ionic strength buffers present during the purification process. Despite this success, excessive degradation of the protein occurred during the long induction period, and the protein could not be concentrated, making it unsuitable for structural studies. By reducing the induction period to 2–3 h at 25 °C and using 1 M NaCl in the purification buffers we have been able to reduce protein degradation and concentrate IcaB$_{Se}^{30-289}$ to >5 mg/ml. Unfortunately this protein was recalcitrant to crystallization. A survey of IcaB homologues from *Staphylococcus*, *Lactobacillus*, and *Bacillus* spp. revealed that they all contain high lysine content (8–15%), which is unfavorable for crystallization. To find an IcaB homologue more suitable for crystallization, an in-depth search using the STRING database (48) for bacterial species with the *icaABCD* operon was performed. This search identified IcaB from *A. degensii*, which has low lysine (4%) and high arginine (8%) content. An IcaB$_{Ad}^{23-280}$ construct lacking the predicted signal sequence was, therefore, constructed and found to fractionate with *E. coli* membranes during purification. Although the protein could be purified when detergent was added to the buffers, it was also recalcitrant to crystallization. Examination of multiple sequence alignments revealed a predicted hydrophobic loop that was only conserved within Gram-positive homologues of IcaB (*i.e.* not within PgaB) (Fig. 1*A*). We predicted that the removal of this loop might improve the stability and solubility of the enzymes and in turn make the protein more amenable to crystallization. Deletion of the predicted hydrophobic loop, residues 56–69 and 50–64 in IcaB$_{Se}$ and IcaB$_{Ad}$, respectively, did not improve the solubility of IcaB$_{Se}^{30-289\Delta loop}$ but greatly improved solubility characteristics of IcaB$_{Ad}^{23-280\Delta loop}$. To determine whether the proposed hydrophobic rich loop was involved in de-*N*-acetylation, fluorescamine assays using PNAG oligomers were completed on all four enzyme constructs. These assays showed no significant differences in activity between IcaB$_{Se}^{30-289}$, IcaB$_{Se}^{30-289\Delta loop}$, IcaB$_{Ad}^{23-280}$, and IcaB$_{Ad}^{23-280\Delta loop}$ (Fig. 1*B*), suggesting that the loop does not play a role in catalysis.

IcaB$_{Ad}^{23-280\Delta loop}$ Is a $(\beta/\alpha)_7$ Barrel with Unique Structural Features—To gain insight into the structure of IcaB, IcaB$_{Ad}^{23-280\Delta loop}$ was subjected to crystallization trials. Crystals were obtained from two different crystallization conditions, and diffraction data were collected to 2.25 and 1.7 Å (crystal 1 and 2, respectively, Table 1). The structure of crystal 1 was solved using molecular replacement with *E. coli* PgaB as the model template (PDB ID 4F9D). Crystal 1 of IcaB$_{Ad}^{23-280\Delta loop}$

TABLE 1
Summary of data collection and refinement statistics
Values in parentheses correspond to the highest resolution shell.

	$IcaB_{Ad}^{23-280\Delta loop}$ Crystal 1	$IcaB_{Ad}^{23-280\Delta loop}$ Crystal 2
Data collection		
Beamline	NSLS X29	NSLS X29
Wavelength (Å)	1.075	1.075
Space group	*I*4	*I*4
Unit-cell parameters (Å)	$a = b = 84.6$, $c = 71.4$	$a = b = 84.5$, $c = 71.9$
Resolution (Å)	50.00-2.25 (2.35-2.25)	50.00-1.70 (1.76-1.70)
Total no. of reflections	173,478	411,607
No. of unique reflections	12,020	28,034
Redundancy	14.7 (10.6)	14.7 (14.6)
Completeness (%)	98.1 (84.7)	100 (100)
Average $I/\sigma(I)$	16.6 (2.8)	60.5 (5.1)
R_{merge} (%)[a]	17.6 (59.5)	8.8 (57.8)
Refinement		
*R*work[b]/*R*free[c]		20.3/23.1
No. of atoms		
Protein		1861
Zn^{2+}		1
Chloride		1
Water		132
Average B-factors (Å^2)[d]		
Protein		45.0
Zn^{2+}		31.9
Chloride		39.6
Water		44.2
Root mean square deviation		
Bond lengths (Å)		0.006
Bond angles (°)		1.09
Ramachandran plot[d]		
Total favored (%)		96.0
Total allowed (%)		99.1
Disallowed (%)		0.9
Coordinate error (Å)[e]		0.22
PDB code		4WCJ

[a] $R_{merge} = \sum\sum|I(k) - \langle I\rangle|/\sum I(k)$, where $I(k)$ and $\langle I\rangle$ represent the diffraction intensity values of the individual measurements and the corresponding mean values. The summation is over all unique measurements.
[b] $R_{work} = \sum||F_{obs}| - k|F_{calc}||/|F_{obs}|$, where F_{obs} and F_{calc} are the observed and calculated structure factors, respectively.
[c] R_{free} is the sum extended over a subset of reflections (7%) excluded from all stages of the refinement.
[d] As calculated using MolProbity (62).
[e] Maximum-Likelihood Based Coordinate Error, as determined by PHENIX (34).

crystallized in the tetragonal space group *I*4 with one molecule in the asymmetric unit. Crystal 2 originally indexed in the space group $P4_2$ and could be solved by molecular replacement using the model from crystal 1. In this space group two IcaB molecules are present in the asymmetric unit. However, density for the second molecule was poor, and the *R* factors could not be refined below 30%. Patterson analysis revealed significant pseudo-translational symmetry with an off-origin peak 96% of the origin peak located at $(x,y,z) = (0.5,0.5,0.5)$ suggesting the true space group was *I*4. Re-indexing the dataset in space group *I*4 produced excellent density maps with one molecule per asymmetric unit and a drop in *R* factors by ~10%. Refinement of crystal 2 produced a final model with good geometry and *R* factors of 20.3% (R_{work}) and 23.1% (R_{free}) (Table 1). Residues 23–30, 278–280, and the hexahistidine tag were not included in the final model as there was no interpretable electron density present.

$IcaB_{Ad}^{23-280\Delta loop}$ adopts a $(\beta/\alpha)_7$ barrel fold common to CE4s (49) (Fig. 2*A*). The core of the structure is composed of seven parallel β-strands arranged in a barrel that is surrounded by seven α-helices with one of the helices capping the bottom of the barrel (Fig. 2*A*). Six loops are present on the top face of the $(\beta/\alpha)_7$ barrel (the C termini of the β-strands) and are important for active site architecture. In addition to the $(\beta/\alpha)_7$ core, three β-hairpins are located in loops L1, L3, and L4, which contain residues important for the formation of the active site groove (Fig. 2*A*). The deleted hydrophobic loop in $IcaB_{Ad}^{23-280\Delta loop}$ is located in loop L1 between Ser-49 and Ser-65 (Fig. 2) and would result in a long structural extension not required for folding the $(\beta/\alpha)_7$ barrel. Electrostatic potential analysis of $IcaB_{Ad}^{23-280\Delta loop}$ reveals two distinct features; first, is an electronegative active site pocket that is along the top of the $(\beta/\alpha)_7$ barrel (Fig. 2*B*). Second, is an electropositive patch located on one side of the $(\beta/\alpha)_7$ barrel near loops L1 and L2, in close proximity to where the deleted hydrophobic loop would extend (Fig. 2*B*).

$IcaB_{Ad}^{23-280\Delta loop}$ Active Site Metal Analysis Suggests an Ordered Zn^{2+}—Examination of $IcaB_{Ad}^{23-280\Delta loop}$ difference electron density maps revealed a large 28σ peak at the top of the $(\beta/\alpha)_7$ barrel, suggesting the presence of a metal ion. The metal ion is coordinated in an octahedral manner by the side chains of Asp-115, His-173, His-178, and three water molecules (Fig. 3*A*). The arrangement of the Asp-His-His residues is characteristic of the metal coordination found in most CE4s. To determine the identity of the metal, anomalous diffraction data were collected on $IcaB_{Ad}^{23-280\Delta loop}$ crystal 1 above and below the absorption edge for the transition metal Zn^{2+}, as it is the most common metal cofactor found in CE4 structures. A significant decrease in anomalous signal was observed for the 28σ peak for the data collected below the Zn^{2+} absorption edge (1.2964 Å) (Fig. 3*B*), confirming the identity of Zn^{2+} as the metal ion.

Previous metal-dependent activity studies on $IcaB_{Se}^{30-289}$ had shown a preference for Zn^{2+} and Co^{2+} in PNAG de-*N*-acetylation. To determine whether $IcaB_{Ad}^{23-280\Delta loop}$ shows the same metal preference as $IcaB_{Se}^{30-289}$, metal-dependent fluorescamine assays were conducted (Fig. 3*C*). $IcaB_{Ad}^{23-280\Delta loop}$ showed similar levels of activity compared with the as-isolated enzyme in the presence of Zn^{2+}, Mn^{2+}, and Fe^{3+} and increases of ~1.3- and 2.3-fold in the presence of Co^{2+} and Ni^{2+}, respectively. Enzyme activity was abolished when incubated with 1 mM EDTA or dipicolinic acid.

Structural Comparison of $IcaB_{Ad}$ and PgaB Reveals the Basis for PNAG Binding—Structural alignment of $IcaB_{Ad}^{23-280\Delta loop}$ with the N-terminal domain of PgaB, residues 43–309 ($PgaB^{43-309}$, PDB ID 4F9D), shows strong conservation of the CE4 domain with a root mean square deviation of 1.7 Å over 219 equivalent Cα atoms (Fig. 4*A*). Two topological differences were found between $IcaB_{Ad}^{23-280\Delta loop}$ and $PgaB^{43-309}$. First, α7 of $IcaB_{Ad}^{23-280\Delta loop}$ is tilted 105° relative to the equivalent α-helix in $PgaB^{43-309}$ (Fig. 4*A*). Second, $IcaB_{Ad}^{23-280\Delta loop}$ only has three β-hairpin motifs (βH1–3), and the loops they reside in (L1, L3, and L4) are much shorter than the equivalent loops in $PgaB^{43-309}$ (Fig. 4*A*). The difference in loop architecture alters the architecture of the active site binding pocket (Fig. 4, *B* and *C*). Residues Tyr-67 and Trp-180 narrow the active site pocket to 10 Å in $IcaB_{Ad}^{23-280\Delta loop}$ as compared with 16 Å in $PgaB^{43-309}$ (Met-67 and Gly-191) (Fig. 4, *B* and *C*). Furthermore, Arg-45 in $IcaB_{Ad}^{23-280\Delta loop}$ is located at the beginning of the cleft at the −1 subsite and would be available for hydrogen bonding to PNAG. The equivalent residue in $PgaB^{43-309}$ is an asparagine (Fig. 1*A*) that is buried in the structure by 3 aromatic residues Phe-66, Tyr-117, and Phe-154.

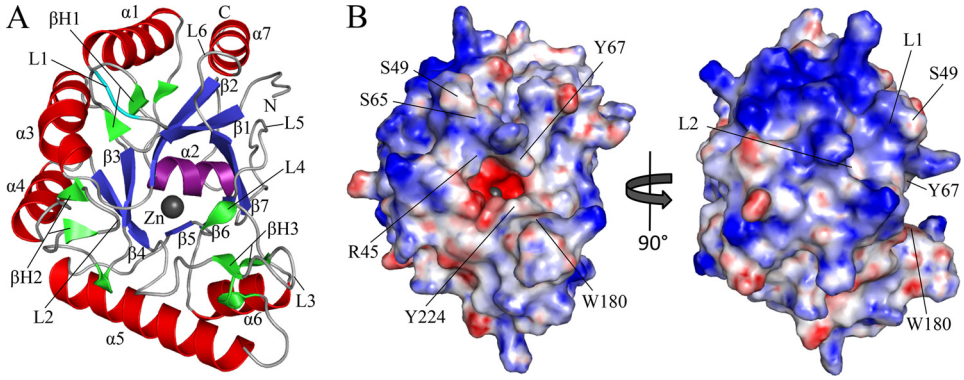

FIGURE 2. **Structure and electrostatic surface representation of $IcaB_{Ad}^{23-280\Delta loop}$.** *A*, $IcaB_{Ad}^{23-280\Delta loop}$ shown in the schematic with the canonical $(\beta/\alpha)_7$ barrel fold labeled β1–7 and α1–7 colored *blue* (β-strands) and *red* (α-helices), respectively, except for the "capping" helix colored *purple* located on the *bottom of the barrel*. Additional secondary structure elements are colored *green* with β-hairpins labeled *βH1–3*, loops labeled *L1–6* and colored *light gray*, and the Zn^{2+} ion colored *dark gray* and shown as a *sphere*. N and C termini are labeled accordingly, and the site where the hydrophobic loop was deleted is colored *cyan*. *B*, electrostatic surface representation of $IcaB_{Ad}^{23-280\Delta loop}$ shown in the same orientation as *panel A* and rotated 90° to the *right* show an electronegative active site pocket and a conserved electropositive patch adjacent to L1 and L2. Quantitative electrostatics are colored from *red* (−10 *kT*/*e*) to *blue* (+10 *kT*/*e*).

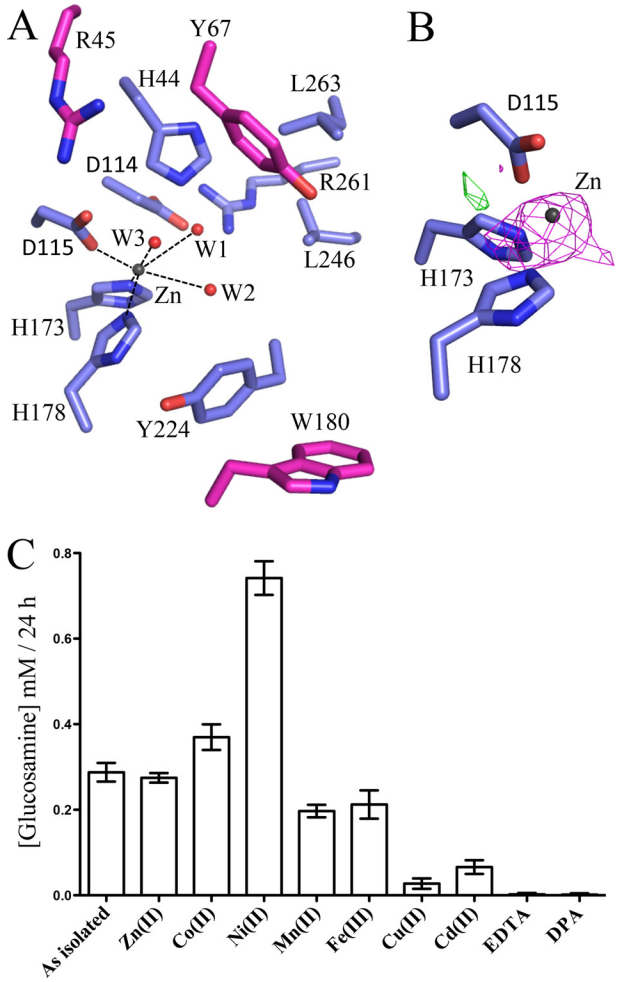

FIGURE 3. **$IcaB_{Ad}^{23-280\Delta loop}$ active site and metal-dependent activity.** *A*, the active site of $IcaB_{Ad}^{23-280\Delta loop}$ is shown in stick representation with the canonical CE4 motif residues, binding groove residues, and the Zn^{2+} ion colored *blue*, *magenta*, and *dark gray*, respectively. *B*, metal coordinating triad of $IcaB_{Ad}^{23-280\Delta loop}$ shown in stick representation (*blue*) with the anomalous difference maps *above* (*magenta*) and *below* (*green*) the Zn^{2+} absorption edge shown as a *mesh* and contoured at 2.0σ. *C*, fluorescamine de-*N*-acetylation activity assay comparison of $IcaB_{Ad}^{23-280\Delta loop}$ (as isolated) and incubated with various divalent metal chlorides or metal chelators. *DPA*, dipicolinic acid. *Bars* represent triplicate experiments with S.D.

Docking Studies with PNAG Oligomers Suggest Three GlcNAc Binding Sites—Docking studies with β-1,6-$(GlcNAc)_3$ and β-1,6-$(GlcNAc)_5$ were conducted using $IcaB_{Ad}^{23-280\Delta loop}$ to gain insight into the determinants for PNAG binding. The predicted affinity for β-1,6-$(GlcNAc)_5$ (−6.0 kcal/mol) was lower than β-1,6-$(GlcNAc)_3$ (−7.2 kcal/mol) in the docking studies, and inspection of the poses computed showed that the first and fifth residues of β-1,6-$(GlcNAc)_5$ (subsites −2 and +2) do not make contacts with $IcaB_{Ad}^{23-280\Delta loop}$. Furthermore, only the top β-1,6-$(GlcNAc)_3$ pose showed hydrogen-bonding contacts with all three *N*-Ac groups to $IcaB_{Ad}^{23-280\Delta loop}$ and thus was used for further analysis. The docked β-1,6-$(GlcNAc)_3$ binds $IcaB_{Ad}^{23-280\Delta loop}$ along the active site groove occupying subsites −1, 0, and +1 (Fig. 5*A*). GlcNAc in the −1 subsite has hydrogen bonds between Arg-45 and Glu-149 to the C5 oxygen (3.6 Å) and *N*-Ac nitrogen (2.9 Å), respectively (Fig. 5*B*). GlcNAc in the 0 subsite makes contacts with the Zn^{2+} ion via the hydroxyl at C3 (OH3) (2.2 Å) and the *N*-Ac carbonyl (2.3 Å), Asp-114 and OH3 (2.7 Å), Arg-45 and OH4 (3.6 Å), and stacking interactions with Tyr-67 (Fig. 5*B*). GlcNAc in the +1 subsite has hydrogen bonds between the backbone carbonyl of Tyr-224 and both the OH3 (3.6 Å) and the *N*-Ac carbonyl (3.5 Å) and T-shaped stacking interactions with Trp-180 (Fig. 5*B*). Interestingly, the *N*-Ac carbonyl and OH3 of the 0 subsite GlcNAc are in close proximity to the crystallographic waters, W2 and W3, with distances of 0.6 and 0.2 Å, respectively (Fig. 5*B*), This observation reinforces the confidence of the docking studies and the positioning of the 0 subsite GlcNAc during catalysis.

Mutational Analysis of IcaB Suggests an Altered CE4 Catalytic Mechanism—CE4s have been proposed to catalyze the deacetylation of their substrates using a metal-assisted general acid and base mechanism (30). The first conserved aspartate found in CE4 motif 1, TFDD, is considered the catalytic base. The conserved histidine in CE4 motif 5, L*X*H, is proposed to be the catalytic acid. From structural and mutational studies on the *Streptococcus pneumoniae* peptidoglycan deacetylase PgdA (30) and the *Vibrio cholerae* chitin deacetylase CDA (31), we hypothesized that His-50/His-44 and Asp-120/Asp-114 are the catalytic acid and base in $IcaB_{Se}$/$IcaB_{Ad}$, respectively. To assess

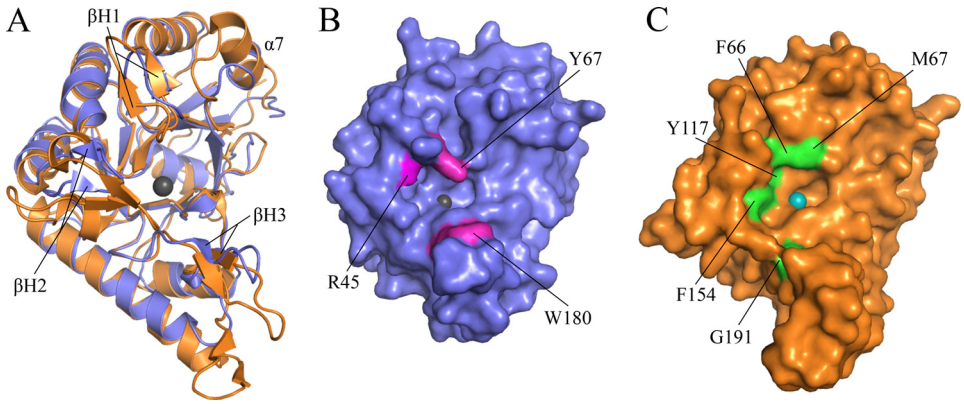

FIGURE 4. **$IcaB_{Ad}$ has a narrow active site pocket compared with $PgaB^{43–309}$.** *A*, superposition of $IcaB_{Ad}^{23–280\Delta loop}$ (*blue*) and $PgaB^{43–309}$ (*orange*) shows a strong conservation of the CE4 fold with a root mean square deviation of 1.7 Å over 219 equivalent Cα atoms. β-Hairpin loops for $IcaB_{Ad}$ are labeled *βH1–3*, and the Zn^{2+} ion is shown as a *sphere colored dark gray*. Surface representation of $IcaB_{Ad}^{23–280\Delta loop}$ (*B*) and $PgaB^{43–309}$ (*C*) is shown in the same representation as *panel A* with residues contributing to the difference in active site architecture colored *magenta* and *green* for $IcaB_{Ad}^{23–280\Delta loop}$ and $PgaB^{43–309}$, respectively. The Ni^{2+} ion in PgaB is shown as a *teal-colored sphere*.

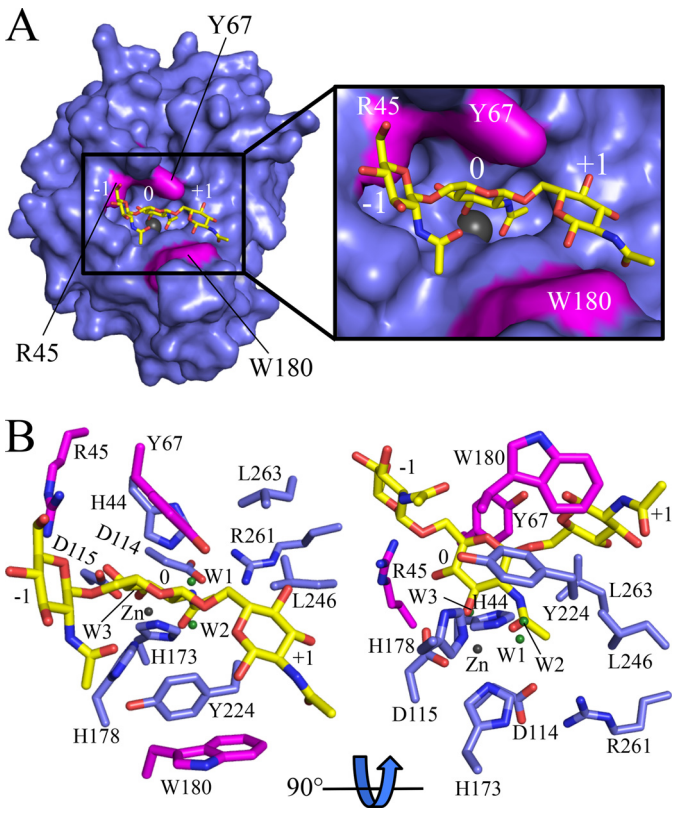

FIGURE 5. **Docking of PNAG oligomers.** *A*, $IcaB_{Ad}^{23–280\Delta loop}$ (*blue*) with a β-1,6-$(GlcNAc)_3$ (*yellow*) docked in the active site shown in surface and stick representations, respectively. The model predicts that Arg-45, Tyr-67, and Trp-180 (*magenta*) are important for the binding of β-1,6-$(GlcNAc)_3$. *B*, active site close-up of the docked β-1,6-$(GlcNAc)_3$ shows the central sugar binds to the Zn^{2+} ion and the crystallographic waters (*W2* and *W3*, *green spheres*) overlap with the *N*-Ac carbonyl and OH-3 oxygens. The Zn^{2+} ion is shown as a *dark gray colored sphere*, and the GlcNAc subsites are labeled from the non-reducing to reducing end as −1, 0, and +1 in both panels.

the role of these residues in the catalytic mechanism H50A/H44A and D120N/D114N variants were assayed for de-*N*-acetylation activity. The histidine variants were completely inactive (Fig. 6*A*), suggesting this conserved residue plays a key role in catalysis. However, the $IcaB_{Se}$ and $IcaB_{Ad}$ aspartate variants displayed 53 and 56% of wild type activity, respectively (Fig. 6*A*), suggesting these residues do not serve essential roles in the catalytic mechanism. Asp-120/Asp-114 may actually be involved in tuning the electrostatics of the active site as the asparagine variants lose their pH activation profile (Fig. 6*B*). To identify a residue in the active site pocket that could potentially serve as the base in the reaction, we used the pK_a prediction server PROPKA3 (50). The predicted pK_a of His-50/His-44 is ~3, suggesting it is basic under the assay conditions and could potentially have a bifunctional role in catalysis (Fig. 6*C*).

The Conserved Hydrophobic Loop of IcaB Is Involved in Membrane Association—The presence of a solvent-accessible hydrophobic loop in Gram-positive homologues of IcaB suggests it may have a functional importance. Given that these proteins are found on the extracellular surface of the bacteria, we hypothesized that the loop may play a role in membrane localization. $IcaB_{Se}^{30–289}$, $IcaB_{Se}^{30–289\Delta loop}$, $IcaB_{Ad}^{23–280}$, and $IcaB_{Ad}^{23–280\Delta loop}$ were, therefore, assayed for their ability to bind and associate with staphylococcal membranes. Using a membrane pulldown assay, $IcaB_{Se}^{30–289}$ and $IcaB_{Ad}^{23–280}$ co-fractioned into the pellet when incubated with staphylococcal membranes (Fig. 7*A*). $IcaB_{Ad}^{23–280\Delta loop}$ was only present in the soluble fraction, and $IcaB_{Se}^{30–289\Delta loop}$ had significantly reduced quantities found in the insoluble fraction (Fig. 7*A*). These data suggest that the hydrophobic loop plays a role in binding and associating with the membrane. Structural modeling of the hydrophobic loop in $IcaB_{Se}^{30–289}$ using Phyre^2 (51) predicts an α-helix spanning residues 59–66 that is amphipathic, with Phe-61, Ile-62, Leu-64, and Leu-65 lying on the solvent exposed face (Fig. 7*B*). A similar result was also seen for Trp-54, Gly-55, Leu-57, and Phe-58 in $IcaB_{Ad}^{23–280}$.

DISCUSSION

IcaB has been identified as an attractive target for the design of inhibitors to combat biofilm-related infections by *S. epidermidis and S. aureus* for two reasons. First, it is an extracellular protein (26), which eliminates the need for membrane permeable drugs. Second, it is responsible for PNAG de-*N*-acetylation, which is required for biofilm formation and virulence in animal models (26, 27). Our recent study of $IcaB_{Se}^{30–289}$ was the first functional characterization of its metal- and length-dependent de-*N*-acetylation activity (32). $IcaB_{Se}$ and its Gram-

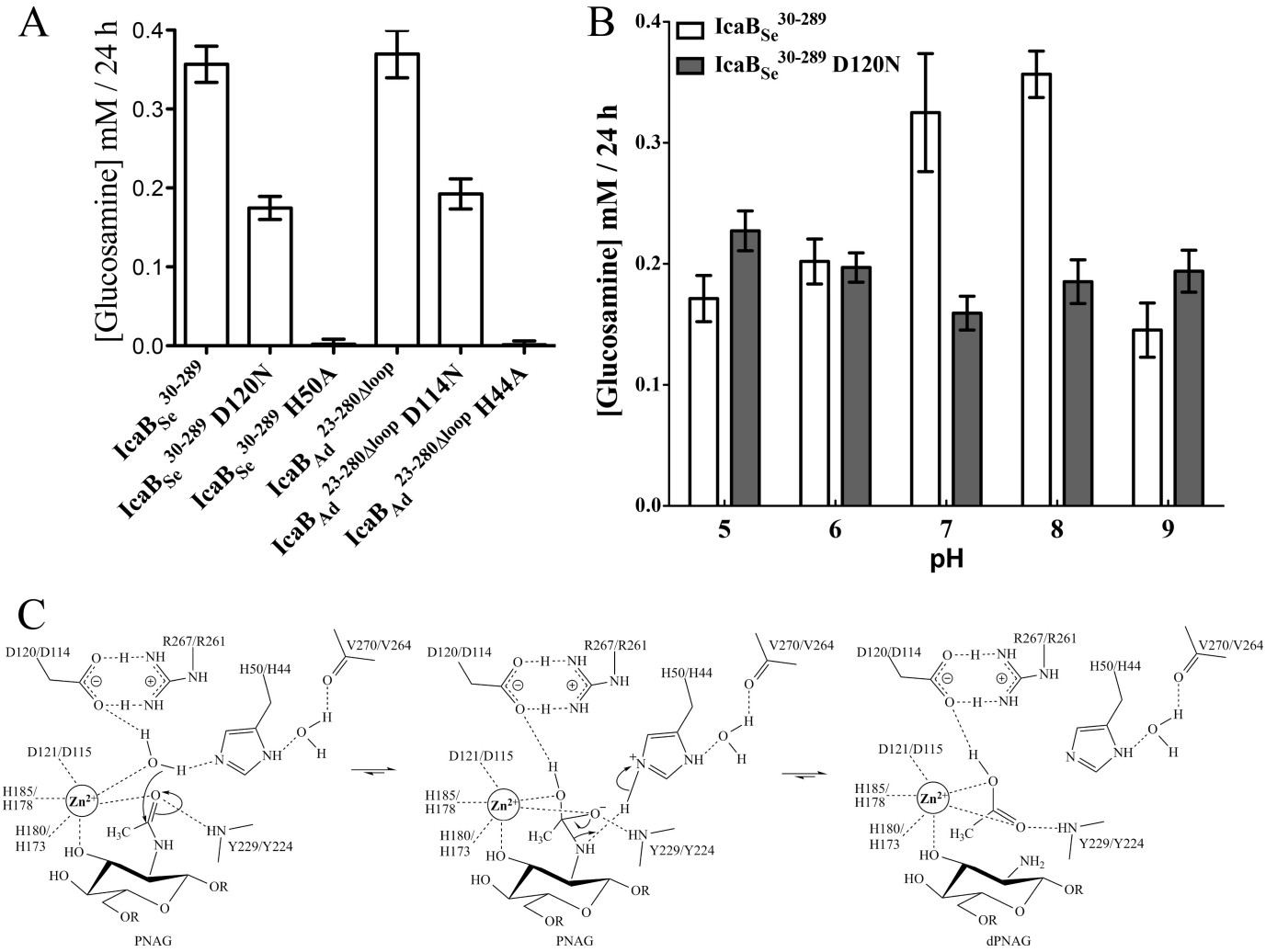

FIGURE 6. **Mutational analysis and proposed catalytic mechanism.** *A*, fluorescamine de-*N*-acetylation activity comparison of wild type $IcaB_{Se}$ and $IcaB_{Ad}$, and their D120N/D114N and H50A/H44A variants. *B*, pH dependence of the fluorescamine de-*N*-acetylation activity of wild type $IcaB_{Se}^{30-289}$ and its D120N variant. *C*, proposed catalytic mechanism for IcaB-dependent de-*N*-acetylation of PNAG. *Bars* represent triplicate experiments with S.D.

negative homologue PgaB have the same enzymatic function but displayed different metal- and length-dependent activity on PNAG oligomers (28, 32). Additionally, the domain architecture and localization of the two proteins are drastically different. $IcaB_{Se}$ is a single-domain extracellular protein, whereas PgaB is a two-domain periplasmic lipoprotein (52, 53).

IcaB contains a hydrophobic loop that is conserved only in Gram-positive homologues (Fig. 1*A*). This hydrophobic loop is not required for de-*N*-acetylation of PNAG oligomers (Fig. 1*B*) but likely contains an amphipathic α-helix that can bind to staphylococcal membranes (Fig. 7). This type of amphipathic α-helix has been found in other integral or associated membrane proteins (54, 55) and is likely, at least in part, responsible for the retention of IcaB to the cell surface. Furthermore, the electropositive patch found on the structure of $IcaB_{Ad}^{23-280\Delta loop}$ (Fig. 2*B*) would be well suited to interact with the negatively charged phosphate groups on the phospholipids and lipoteichoic acids. This correlates well with previous *in vivo* data that shows $IcaB_{Se}$ as a membrane-associated extracellular protein (26).

$IcaB_{Ad}^{23-280\Delta loop}$ contains an Asp-His-His triad that coordinates an ordered Zn^{2+} ion in the structure (Fig. 3*B*). $IcaB_{Ad}^{23-280\Delta loop}$ displays metal-dependent de-*N*-acetylation of PNAG oligomers with a preference for Ni^{2+}, Co^{2+}, and Zn^{2+} (Fig. 3*C*). PgaB displayed the highest activity with Co^{2+} and Ni^{2+} cofactors (28), whereas $IcaB_{Se}^{30-289}$ had the highest activity with Co^{2+} and Zn^{2+} (32). The metal ion promiscuity in IcaB appears to be a continuing trend for the CE4 family. $IcaB_{Ad}^{23-280\Delta loop}$ shows structural similarity to $PgaB^{43-309}$ and contains the same circularly permuted arrangement of the CE4 motifs, a feature unique to these CE4 members (28, 56). Despite the high structural similarity and metal ion preference between IcaB and $PgaB^{43-309}$, only IcaB is enzymatically active on PNAG oligomers; PgaB requires both N- and C-terminal domains for de-*N*-acetylation activity (29). Structural studies on CDA and comparison to known CE4 structures reveals that loop architecture plays a major role in substrate binding and the enzymatic mechanism (31). The loop architecture of $IcaB_{Ad}^{23-280\Delta loop}$ is similar to other CE4s, like PgdA (30), which has a narrow binding pocket. Additionally, the conserved residues Arg-45, Tyr-67, and Trp-180 make important interactions with the three GlcNAc moieties at -1, 0, and $+1$ subsites, respectively, in the docking studies (Fig. 5). $PgaB^{43-309}$ does not contain any of

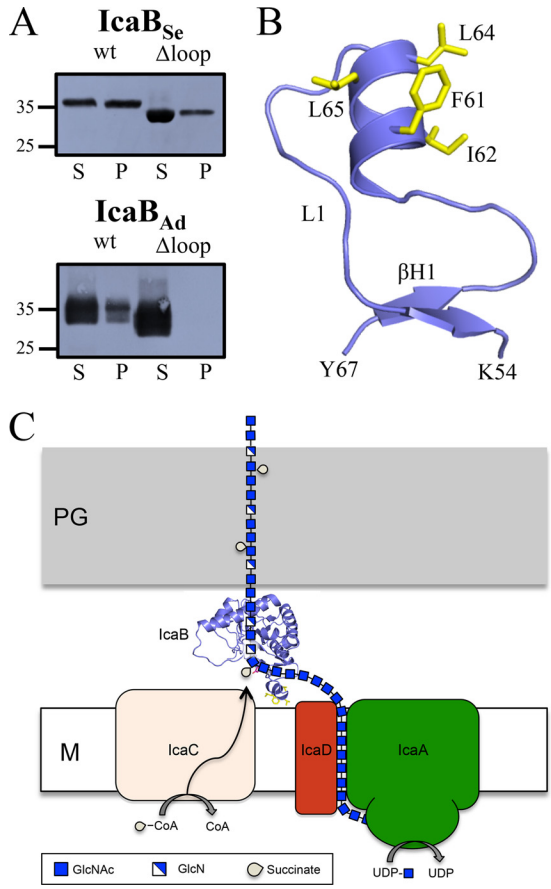

FIGURE 7. **Membrane localization of IcaB.** *A*, staphylococcal membrane pulldown assays of purified IcaB proteins show the hydrophobic loop is important for membrane association. *S*, supernatant; *P*, pellet; *wt*, wild type. Molecular mass markers are indicated on the *left side of the blots* in kDa. *B*, predicted structure for the IcaB$_{Se}$ hydrophobic loop reveals an amphipathic α-helix. *C*, proposed model for PNAG biosynthesis and modification. IcaB associates with the membrane via its hydrophobic loop and electropositive surface and de-*N*-acetylates PNAG after export. *M*, membrane; *PG*, peptidoglycan; *CoA*, coenzyme A.

these conserved elements (Fig. 4, *A* and *C*), likely leading to loss of PNAG binding and thus rendering the isolated domain inactive. Previous docking and simulation studies have suggested that conserved elements, including a conserved arginine and tryptophan, on PgaB$^{310-672}$ are required for PNAG binding and catalysis in the *E. coli* enzyme (29). The cleft formed between the two domains of PgaB also creates a long extended active site (29). This correlates with the enzymatic data that shows length-dependent de-*N*-acetylation of the oligosaccharides up to β-1,6-(GlcNAc)$_5$ with preference for the central GlcNAc (28). The structure of IcaB$_{Ad}^{23-280\Delta loop}$ suggests only three GlcNAc subsites within the active site pocket (Fig. 5). This is supported by previous studies with IcaB$_{Se}^{30-289}$ that showed similar de-*N*-acetylation of β-1,6-(GlcNAc)$_3$ to β-1,6-(GlcNAc)$_6$ and displayed deacetylation preference at the second GlcNAc from the reducing end (32). The involvement of PgaB$^{310-672}$ during de-*N*-acetylation appears to be part of a mechanism for PgaB to continuously associate with the dPNAG polymer (29). This type of processive mechanism would produce an energetically favorable extended state of dPNAG to allow for efficient periplasmic translocation and hand-off to the export machinery (29). Because IcaB is an extracellular protein it does not need an auxiliary domain for continual processing and export of dPNAG. It is probable that IcaB will interact with dPNAG multiple times as they both are present in the extracellular matrix. This is consistent with the higher levels of deacetylation observed for *S. epidermidis* (~15–20%) over *E. coli* (~3–5%) in dPNAG isolated from source even though IcaB displays lower levels of activity than PgaB *in vitro*. The circular permutation of the CE4 motifs in IcaB and PgaB must play a role other than substrate binding during catalysis. PgaB has been proposed to operate through a similar enzymatic mechanism to other CE4 members (57) but is lacking a key catalytic residue that has been proposed to attenuate its catalytic efficiency (28). Our preliminary mutational analysis suggests Asp-120/Asp-114 is not the catalytic base as the equivalent D275N variant in PgdA inactivates the enzyme. In the IcaB$_{Ad}^{23-280\Delta loop}$ structure Asp-114 is in a bi-dentate salt bridge with Arg-261 (Asp-120 and Arg-267 in IcaB$_{Se}$), which would prevent a free carboxylate group that could serve as the base. The equivalent salt bridge in both PgdA and CDA are not bi-dentate as the conserved arginine spans the active site in a different orientation. This would free the aspartate carboxylate group to abstract a proton from the nucleophilic water. Thus, we propose His-50/His-44 to be a bifunctional acid base catalyst in the enzymatic mechanism (Fig. 6*C*). In our proposed scheme, hydrolysis of the 0 subsite GlcNAc *N*-Ac group would be initiated by the Zn^{2+}-coordinated water molecule. Deprotonation of the water by His-50/His-44 would lead to nucleophilic attack of the *N*-Ac carbonyl group to produce a tetrahedral oxyanion intermediate that would be stabilized by the Zn^{2+} ion and the backbone amide of Tyr-229/Tyr-224. The intermediate would then be protonated on the *N*-Ac nitrogen by the imidazolium of His-50/His-44. This would generate a free amine leaving group (dPNAG) and the acetic acid byproduct. Diffusion of acetic acid out and water into the active site would regenerate the enzyme and lead to another round of de-*N*-acetylation on the dPNAG polymer. Similar bifunctional roles have been proposed for a glutamic acid in the zinc metalloamidases LpxC (58, 59) and carboxypeptidase A (60, 61). Together, these results suggest that the circular permutation of the CE4 motifs in IcaB and its Gram-negative homologue PgaB may result in an altered CE4 enzymatic mechanism.

The structure, functional characterization, and membrane association of IcaB reported here will help facilitate additional studies that probe our proposed model for the biosynthesis and modification of PNAG in Gram-positive bacteria (Fig. 7*C*) and will help guide the development of novel inhibitors to prevent biofilm-related infection caused by *S. epidermidis* and *S. aureus*.

Acknowledgments—We thank Patrick Yip for technical assistance and the Trimble laboratory at The Hospital for Sick Children for the use of their micro-ultracentrifuge. The National Synchrotron Light Source beam line X29A is supported by the United States Department of Energy Office of Biological and Environmental Research and the National Institutes of Health National Centre for Research Resources.

REFERENCES

1. O'Gara, J. P., and Humphreys, H. (2001) *Staphylococcus epidermidis* biofilms: importance and implications. *J. Med. Microbiol.* **50,** 582–587
2. von Eiff, C., Peters, G., and Heilmann, C. (2002) Pathogenesis of infections due to coagulase-negative staphylococci. *Lancet Infect. Dis.* **2,** 677–685
3. Rohde, H., Frankenberger, S., Zähringer, U., and Mack, D. (2010) Structure, function, and contribution of polysaccharide intercellular adhesin (PIA) to *Staphylococcus epidermidis* biofilm formation and pathogenesis of biomaterial-associated infections. *Eur. J. Cell Biol.* **89,** 103–111
4. Hall-Stoodley, L., Costerton, J. W., and Stoodley, P. (2004) Bacterial biofilms: from the natural environment to infectious diseases. *Nat. Rev. Microbiol.* **2,** 95–108
5. López, D., Vlamakis, H., and Kolter, R. (2010) Biofilms. *Cold Spring Harb. Perspect. Biol.* **2,** a000398
6. Sutherland, I. (2001) Biofilm exopolysaccharides: a strong and sticky framework. *Microbiology* **147,** 3–9
7. Vu, B., Chen, M., Crawford, R. J., and Ivanova, E. P. (2009) Bacterial extracellular polysaccharides involved in biofilm formation. *Molecules* **14,** 2535–2554
8. Branda, S. S., Vik, S., Friedman, L., and Kolter, R. (2005) Biofilms: the matrix revisited. *Trends Microbiol.* **13,** 20–26
9. Sutherland, I. W. (2001) The biofilm matrix: an immobilized but dynamic microbial environment. *Trends Microbiol.* **9,** 222–227
10. Zhao, K., Tseng, B. S., Beckerman, B., Jin, F., Gibiansky, M. L., Harrison, J. J., Luijten, E., Parsek, M. R., and Wong, G. C. (2013) Psl trails guide exploration and microcolony formation in *Pseudomonas aeruginosa* biofilms. *Nature* **497,** 388–391
11. Mack, D., Fischer, W., Krokotsch, A., Leopold, K., Hartmann, R., Egge, H., and Laufs, R. (1996) The intercellular adhesin involved in biofilm accumulation of *Staphylococcus epidermidis* is a linear β-1,6-linked glucosaminoglycan: purification and structural analysis. *J. Bacteriol.* **178,** 175–183
12. McKenney, D., Pouliot, K. L., Wang, Y., Murthy, V., Ulrich, M., Döring, G., Lee, J. C., Goldmann, D. A., and Pier, G. B. (1999) Broadly protective vaccine for *Staphylococcus aureus* based on an in vivo-expressed antigen. *Science* **284,** 1523–1527
13. Wang, X., Preston, J. F., 3rd, and Romeo, T. (2004) The pgaABCD locus of *Escherichia coli* promotes the synthesis of a polysaccharide adhesin required for biofilm formation. *J. Bacteriol.* **186,** 2724–2734
14. Choi, A. H., Slamti, L., Avci, F. Y., Pier, G. B., and Maira-Litrán, T. (2009) The pgaABCD locus of *Acinetobacter baumannii* encodes the production of poly-β-1–6-*N*-acetylglucosamine, which is critical for biofilm formation. *J. Bacteriol.* **191,** 5953–5963
15. Sloan, G. P., Love, C. F., Sukumar, N., Mishra, M., and Deora, R. (2007) The *Bordetella* Bps polysaccharide is critical for biofilm development in the mouse respiratory tract. *J. Bacteriol.* **189,** 8270–8276
16. Conover, M. S., Sloan, G. P., Love, C. F., Sukumar, N., and Deora, R. (2010) The Bps polysaccharide of *Bordetella pertussis* promotes colonization and biofilm formation in the nose by functioning as an adhesin. *Mol. Microbiol.* **77,** 1439–1455
17. Izano, E. A., Sadovskaya, I., Vinogradov, E., Mulks, M. H., Velliyagounder, K., Ragunath, C., Kher, W. B., Ramasubbu, N., Jabbouri, S., Perry, M. B., and Kaplan, J. B. (2007) Poly-*N*-acetylglucosamine mediates biofilm formation and antibiotic resistance in *Actinobacillus pleuropneumoniae*. *Microb. Pathog.* **43,** 1–9
18. Jarrett, C. O., Deak, E., Isherwood, K. E., Oyston, P. C., Fischer, E. R., Whitney, A. R., Kobayashi, S. D., DeLeo, F. R., and Hinnebusch, B. J. (2004) Transmission of *Yersinia pestis* from an infectious biofilm in the flea vector. *J. Infect. Dis.* **190,** 783–792
19. Yakandawala, N., Gawande, P. V., LoVetri, K., Cardona, S. T., Romeo, T., Nitz, M., and Madhyastha, S. (2011) Characterization of the poly-β-1,6-*N*-acetylglucosamine polysaccharide component of *Burkholderia* biofilms. *Appl. Environ. Microbiol.* **77,** 8303–8309
20. Cywes-Bentley, C., Skurnik, D., Zaidi, T., Roux, D., Deoliveira, R. B., Garrett, W. S., Lu, X., O'Malley, J., Kinzel, K., Zaidi, T., Rey, A., Perrin, C., Fichorova, R. N., Kayatani, A. K., Maira-Litràn, T., Gening, M. L., Tsvetkov, Y. E., Nifantiev, N. E., Bakaletz, L. O., Pelton, S. I., Golenbock, D. T., and Pier, G. B. (2013) Antibody to a conserved antigenic target is protective against diverse prokaryotic and eukaryotic pathogens. *Proc. Natl. Acad. Sci. U.S.A.* **110,** E2209–E2218
21. Heilmann, C., Schweitzer, O., Gerke, C., Vanittanakom, N., Mack, D., and Götz, F. (1996) Molecular basis of intercellular adhesion in the biofilm-forming *Staphylococcus epidermidis*. *Mol. Microbiol.* **20,** 1083–1091
22. Gerke, C., Kraft, A., Süssmuth, R., Schweitzer, O., and Götz, F. (1998) Characterization of the *N*-acetylglucosaminyltransferase activity involved in the biosynthesis of the *Staphylococcus epidermidis* polysaccharide intercellular adhesin. *J. Biol. Chem.* **273,** 18586–18593
23. Atkin, K. E., MacDonald, S. J., Brentnall, A. S., Potts, J. R., and Thomas, G. H. (2014) A different path: revealing the function of staphylococcal proteins in biofilm formation. *FEBS Lett.* **588,** 1869–1872
24. Sadovskaya, I., Vinogradov, E., Flahaut, S., Kogan, G., and Jabbouri, S. (2005) Extracellular carbohydrate-containing polymers of a model biofilm-producing strain, *Staphylococcus epidermidis* RP62A. *Infect. Immun.* **73,** 3007–3017
25. Joyce, J. G., Abeygunawardana, C., Xu, Q., Cook, J. C., Hepler, R., Przysiecki, C. T., Grimm, K. M., Roper, K., Ip, C. C., Cope, L., Montgomery, D., Chang, M., Campie, S., Brown, M., McNeely, T. B., Zorman, J., Maira-Litrán, T., Pier, G. B., Keller, P. M., Jansen, K. U., and Mark, G. E. (2003) Isolation, structural characterization, and immunological evaluation of a high-molecular-weight exopolysaccharide from *Staphylococcus aureus*. *Carbohydr. Res.* **338,** 903–922
26. Vuong, C., Kocianova, S., Voyich, J. M., Yao, Y., Fischer, E. R., DeLeo, F. R., and Otto, M. (2004) A crucial role for exopolysaccharide modification in bacterial biofilm formation, immune evasion, and virulence. *J. Biol. Chem.* **279,** 54881–54886
27. Cerca, N., Jefferson, K. K., Maira-Litrán, T., Pier, D. B., Kelly-Quintos, C., Goldmann, D. A., Azeredo, J., and Pier, G. B. (2007) Molecular basis for preferential protective efficacy of antibodies directed to the poorly acetylated form of staphylococcal poly-*N*-acetyl-β-(1–6)-glucosaminev. *Infect. Immun.* **75,** 3406–3413
28. Little, D. J., Poloczek, J., Whitney, J. C., Robinson, H., Nitz, M., and Howell, P. L. (2012) The structure- and metal-dependent activity of *Escherichia coli* PgaB provides insight into the partial de-*N*-acetylation of poly-β-1,6-*N*-acetyl-D-glucosamine. *J. Biol. Chem.* **287,** 31126–31137
29. Little, D. J., Li, G., Ing, C., DiFrancesco, B. R., Bamford, N. C., Robinson, H., Nitz, M., Pomès, R., and Howell, P. L. (2014) Modification and periplasmic translocation of the biofilm exopolysaccharide poly-β-1,6-*N*-acetyl-D-glucosamine. *Proc. Natl. Acad. Sci. U.S.A.* **111,** 11013–11018
30. Blair, D. E., Schüttelkopf, A. W., MacRae, J. I., and van Aalten, D. M. (2005) Structure- and metal-dependent mechanism of peptidoglycan deacetylase, a streptococcal virulence factor. *Proc. Natl. Acad. Sci. U.S.A.* **102,** 15429–15434
31. Andrés, E., Albesa-Jové, D., Biarnés, X., Moerschbacher, B. M., Guerin, M. E., and Planas, A. (2014) Structural basis of chitin oligosaccharide deacetylation. *Angew. Chem. Int. Ed. Engl.* **53,** 6882–6887
32. Pokrovskaya, V., Poloczek, J., Little, D. J., Griffiths, H., Howell, P. L., and Nitz, M. (2013) Functional characterization of *Staphylococcus epidermidis* IcaB, a de-*N*-acetylase important for biofilm formation. *Biochemistry* **52,** 5463–5471
33. Otwinowski, Z., and Minor, W. (1997) Processing of x-ray diffraction data collected in oscillation mode. *Methods Enzymol.* **276,** 307–326
34. Adams, P. D., Afonine, P. V., Bunkóczi, G., Chen, V. B., Davis, I. W., Echols, N., Headd, J. J., Hung, L. W., Kapral, G. J., Grosse-Kunstleve, R. W., McCoy, A. J., Moriarty, N. W., Oeffner, R., Read, R. J., Richardson, D. C., Richardson, J. S., Terwilliger, T. C., and Zwart, P. H. (2010) PHENIX: a comprehensive Python-based system for macromolecular structure solution. *Acta Crystallogr. D Biol. Crystallogr.* **66,** 213–221
35. Emsley, P., and Cowtan, K. (2004) Coot: model-building tools for molecular graphics. *Acta Crystallogr. D Biol. Crystallogr.* **60,** 2126–2132
36. Painter, J., and Merritt, E. A. (2006) Optimal description of a protein structure in terms of multiple groups undergoing TLS motion. *Acta Crystallogr. D Biol. Crystallogr.* **62,** 439–450
37. Painter, J., and Merritt, E. A. (2006) TLSMD web server for the generation of multi-group TLS models. *J. Appl. Crystallogr.* **39,** 109–111
38. Dolinsky, T. J., Czodrowski, P., Li, H., Nielsen, J. E., Jensen, J. H., Klebe, G., and Baker, N. A. (2007) PDB ID 2PQR: expanding and upgrading auto-

mated preparation of biomolecular structures for molecular simulations. *Nucleic Acids Res.* **35,** W522–W525
39. Dolinsky, T. J., Nielsen, J. E., McCammon, J. A., and Baker, N. A. (2004) PDB ID 2PQR: an automated pipeline for the setup of Poisson-Boltzmann electrostatics calculations. *Nucleic Acids Res.* **32,** W665–W667
40. Baker, N. A., Sept, D., Joseph, S., Holst, M. J., and McCammon, J. A. (2001) Electrostatics of nanosystems: application to microtubules and the ribosome. *Proc. Natl. Acad. Sci. U.S.A.* **98,** 10037–10041
41. Morin, A., Eisenbraun, B., Key, J., Sanschagrin, P. C., Timony, M. A., Ottaviano, M., and Sliz, P. (2013) Collaboration gets the most out of software. *eLife* **2,** e01456
42. Winn, M. D., Ballard, C. C., Cowtan, K. D., Dodson, E. J., Emsley, P., Evans, P. R., Keegan, R. M., Krissinel, E. B., Leslie, A. G., McCoy, A., McNicholas, S. J., Murshudov, G. N., Pannu, N. S., Potterton, E. A., Powell, H. R., Read, R. J., Vagin, A., and Wilson, K. S. (2011) Overview of the CCP4 suite and current developments. *Acta Crystallogr. D Biol. Crystallogr.* **67,** 235–242
43. Trott, O., and Olson, A. J. (2010) AutoDock Vina: improving the speed and accuracy of docking with a new scoring function, efficient optimization, and multithreading. *J. Comput. Chem.* **31,** 455–461
44. Woods Group (2005–2014) GLYCAM Web. Complex Carbohydrate Research Center, University of Georgia, Athens, GA
45. Sanner, M. F. (1999) Python: a programming language for software integration and development. *J. Mol. Graph. Model.* **17,** 57–61
46. Leung, C., Chibba, A., Gómez-Biagi, R. F., and Nitz, M. (2009) Efficient synthesis and protein conjugation of β-(1→6)-D-*N*-acetylglucosamine oligosaccharides from the polysaccharide intercellular adhesin. *Carbohydr. Res.* **344,** 570–575
47. Udenfriend, S., Stein, S., Böhlen, P., Dairman, W., Leimgruber, W., and Weigele, M. (1972) Fluorescamine: a reagent for assay of amino acids, peptides, proteins, and primary amines in the picomole range. *Science* **178,** 871–872
48. Snel, B., Lehmann, G., Bork, P., and Huynen, M. A. (2000) STRING: a web-server to retrieve and display the repeatedly occurring neighbourhood of a gene. *Nucleic Acids Res.* **28,** 3442–3444
49. Blair, D. E., and van Aalten, D. M. (2004) Structures of *Bacillus subtilis* PdaA, a family 4 carbohydrate esterase, and a complex with *N*-acetylglucosamine. *FEBS Lett.* **570,** 13–19
50. Olsson, M., and Søndergaard, C. R. (2011) PROPKA3: consistent treatment of internal and surface residues in empirical pKa predictions. *J. Chem. Theory Comput.* **7,** 525–537
51. Kelley, L. A., and Sternberg, M. J. (2009) Protein structure prediction on the Web: a case study using the Phyre server. *Nat Protoc* **4,** 363–371
52. Itoh, Y., Rice, J. D., Goller, C., Pannuri, A., Taylor, J., Meisner, J., Beveridge, T. J., Preston, J. F., 3rd, and Romeo, T. (2008) Roles of pgaABCD genes in synthesis, modification, and export of the *Escherichia coli* biofilm adhesin, poly-β-1,6-*N*-acetyl-D-glucosamine (PGA). *J. Bacteriol.* **190,** 3670–3680
53. Little, D. J., Whitney, J. C., Robinson, H., Yip, P., Nitz, M., and Howell, P. L. (2012) Combining in situ proteolysis and mass spectrometry to crystallize *Escherichia coli* PgaB. *Acta Crystallogr Sect. F. Struct. Biol. Cryst. Commun.* **68,** 842–845
54. Lovering, A. L., Lin, L. Y., Sewell, E. W., Spreter, T., Brown, E. D., and Strynadka, N. C. (2010) Structure of the bacterial teichoic acid polymerase TagF provides insights into membrane association and catalysis. *Nat. Struct. Mol. Biol.* **17,** 582–589
55. Bracey, M. H., Hanson, M. A., Masuda, K. R., Stevens, R. C., and Cravatt, B. F. (2002) Structural adaptations in a membrane enzyme that terminates endocannabinoid signaling. *Science* **298,** 1793–1796
56. Nishiyama, T., Noguchi, H., Yoshida, H., Park, S. Y., and Tame, J. R. (2013) The structure of the deacetylase domain of *Escherichia coli* PgaB, an enzyme required for biofilm formation: a circularly permuted member of the carbohydrate esterase 4 family. *Acta Crystallogr. D Biol. Crystallogr.* **69,** 44–51
57. Little, D. J., Bamford, N. C., Nitz, M., and Howell, P. L. (2014) Metal-dependent polysaccharide deacetylase PgaB. *Encyclopedia of Inorganic and Bioinorganic Chemistry* (Scott, R.A., ed.) pp. 1–11, John Wiley & Sons, Inc., Chichester, UK
58. Whittington, D. A., Rusche, K. M., Shin, H., Fierke, C. A., and Christianson, D. W. (2003) Crystal structure of LpxC, a zinc-dependent deacetylase essential for endotoxin biosynthesis. *Proc. Natl. Acad. Sci. U.S.A.* **100,** 8146–8150
59. Hernick, M., and Fierke, C. A. (2005) Zinc hydrolases: the mechanisms of zinc-dependent deacetylases. *Arch. Biochem. Biophys.* **433,** 71–84
60. Christianson, D. W., David, P. R., and Lipscomb, W. N. (1987) Mechanism of carboxypeptidase A: hydration of a ketonic substrate analogue. *Proc. Natl. Acad. Sci. U.S.A.* **84,** 1512–1515
61. Christianson, D. W., and Lipscomb, W. N. (1989) Carboxypeptidase A. *Acc. Chem. Res.* **22,** 62–69
62. Chen, V. B., Arendall, W. B., 3rd, Headd, J. J., Keedy, D. A., Immormino, R. M., Kapral, G. J., Murray, L. W., Richardson, J. S., and Richardson, D. C. (2010) MolProbity: all-atom structure validation for macromolecular crystallography. *Acta Crystallogr. D Biol. Crystallogr.* **66,** 12–21